Design and control methodology of a 3-DOF flexure-based mechanism for micro/nano positioning

Z. Guo[1], Y. Tian[1], C. Liu[1], F. Wang[1], X. Liu[2], B. Shirinzadeh[3], D. Zhang[1]

[1]Key Laboratory of Mechanism Theory and Equipment Design of Ministry of Education, Tianjin University, Tianjin 300072, China

[2]School of Engineering, University of Warwick, Coventry CV4 7AL, UK

[3]Robotics and Mechatronics Research Laboratory, Department of Mechanical and Aerospace Engineering, Monash University, VIC 3800, Australia

Abstract: A 3-DOF (X-Y-θ_Z) planar flexure-based mechanism is designed and monolithically manufactured using WEDM (Wire Electro-Discharge Machining) technology. The compact flexure-based mechanism is directly driven by three piezoelectric actuators (PZTs) through decoupling mechanisms. The orthogonal configuration in the x and y directions can guarantee the decoupling translational motion in these axes. The rotational motion and translational displacement in the x direction can be decoupled by controlling the piezoelectric actuators in the x axis with the same displacement values in same and opposite motion directions, respectively. The static and dynamic models of the developed flexure-based mechanism have been developed based on the pseudo-rigid-body model methodology. The mechanical design optimization is conducted to improve the static and dynamic characteristics of the flexure-based mechanism. Finite Element Analyses (FEA) are also carried out to verify the established models and optimization results. A novel hybrid feedforward/feedback controller has been provided to eliminate/reduce the nonlinear hysteresis and external disturbance of the flexure-based mechanism. Experimental testing has been performed to examine the dynamic performance of the developed flexure-based mechanism.

Keywords: flexure-based mechanism, static analysis, dynamic analysis, optimization design, hybrid control.

1. Introduction

Micro/nano positioning technology is one of the key enabling methodologies for modern scientific and engineering applications including AFM (Atomic Force Microscopy), STM (Scanning Tunnel Microscopy), optical fiber alignment, bio-micro-surgery, bio-nanotechnology, and micro/nano assembly and manipulation [1-5]. It is well known that the static and dynamic characteristics of the micro/nano positioning mechanisms are mainly dependent on the structure of the mechanism and the performance of the actuator [6]. Among the available types of actuators, piezoelectric actuator is one of the best choices for the micro/nano positioning mechanisms due to the infinite resolution, high stiffness, and large bandwidth. In order to implement nanometer level positioning with high resolution and smooth motion, the stick-slip phenomenon of the traditional kinematic pair must be avoided. To solve this problem, flexure-based mechanisms are generally utilized to guide the motion of the platform. Since flexure hinges have a number of advantages including no friction, no backlash, free of lubrication [7, 8].

Recent research efforts have been directed towards the mechanical design optimization of planar flexure-based mechanisms which can be divided into two categories, namely serial kinematic mechanisms [9, 10] and parallel kinematic mechanisms [11-14]. The motion of each axis can be independently measured and controlled in the serial kinematic mechanisms, and thus it is easy to construct and implement. However, the assembly error and different dynamic performance in different motion axes are the shortcomings of such kinds of mechanisms. On the contrary, the parallel kinematic mechanisms have a number of advantages including structural compactness and high stiffness. But the motion cross coupling, complex kinematic equation and small workspace are the bottleneck to block the practical applications of these kinds of mechanisms. Thus, it is necessary to develop the decoupling flexure-based mechanisms for micro/nano positioning technology.

For the planar micro/nano positioning, 2-DOF (Degree of Freedom) mechanism is an essential requirement for most of the academic and industrial applications. However, the orientation adjustment is also crucial for the alignment of micro/nano objects. Thus, 3-DOF planar micro/nano positioning mechanisms should be developed to fulfill the demands. A number of flexure-based parallel mechanisms have been developed to implement micro/nano manipulation [15-18]. To enlarge the workspace of the developed flexure-based mechanisms, a lever mechanism is generally utilized to amplify the output displacement of the piezoelectric actuator. This will improve the structural complexity of the mechanisms and reduce the bandwidth of the entire system.

Besides the mechanical design and optimization of the flexure-based mechanisms, the elimination/reduction of the nonlinear hysteresis of piezoelectric actuators plays another important role in the micro/nano positioning systems. Thus, it is necessary to establish the hysteresis model of the piezoelectric actuator for the output displacement compensation. There are many hysteresis models developed in the literature. PI (Prandtl-Ishlinskii) hysteresis model is one of the attractive candidates for its structural simplicity and analytical inverse model [19, 20]. Based on the developed inverse PI hysteresis model, a feedforward controller can be constructed to compensate the nonlinearity of the piezoelectric actuator [21, 22]. In order to eliminate/reduce the external disturbance and further improve the positioning accuracy of the micro/nano positioning mechanism, a feedback controller is usually adopted to form the combined feedforward/feedback control of such kinds of micro/nano positioning mechanisms [7, 23, 24]. However, the performance of the feedforward controller has significantly influence on the entire system. To improve the control accuracy and robust of the feedforward controller, the common method is to increase the number of the backlash operator and/or the dead-zone operator. This will increase the complexity of the inverse PI model and thus enlarge the response time of the entire control system. Therefore, it is crucial to develop a novel feedforward controller to meet the requirement.

In this paper, a 3-DOF (X-Y-θ_Z) planar flexure-based mechanism is designed and monolithically manufactured using WEDM (Wire Electro-Discharge Machining) technology. The compact flexure-based mechanism is directly driven by three piezoelectric actuators through decoupling mechanisms. The orthogonal configuration in x and y directions can guarantee the decoupling translational motion in these axes. The rotational motion and translational displacement in the x direction can be decoupled by controlling the piezoelectric actuators in the x axis with the same displacement values in same and opposite motion directions, respectively. The static and dynamic models of the developed flexure-based mechanism have been developed based on the pseudo-rigid-body model methodology. The mechanical design optimization is conducted to improve the static and dynamic characteristics of the flexure-based mechanism. Finite Element Analyses (FEA) is also carried out to verify the established models and optimization results. A novel hybrid feedforward/feedback controller has been provided to eliminate/reduce the nonlinear hysteresis and external disturbance of the flexure-based mechanism. Experimental testing has been performed to examine the dynamic performance of the developed flexure-based mechanism.

2. Mechanical design

The schematic diagram of the 3-DOF (X-Y-θ_Z) flexure-based mechanism is shown in Fig.1. There is one piezoelectric actuator in y direction, and are two parallel mounted piezoelectric actuators in x direction. The translational motion can be implemented by controlling the displacement of piezoelectric actuator 1 and piezoelectric actuators 2 & 3 simultaneously, respectively. The rotational motion can be implemented by providing opposite displacement to the piezoelectric actuators 2 & 3 which are firstly inputted into an initial voltage. The orthogonal configuration of piezoelectric actuators can implement the decoupling motion in the x and y directions within the working range from a few nanometers to several micrometer level. As shown in Fig. 1(b), six Double Circular Hinge Linkages (DCHL) are used to translate the driving force and to decouple the motion, as well as to support the moving platform of the flexure-based mechanism. Due to the brittle material of the ceramics, bending and torsional moments will damage the piezoelectric actuator. Thus, the Dual Leaf Parallelogram Hinge (DLPH), as shown in Fig. 1(c), is utilized to guide the motion of the piezoelectric actuator, and further the half cylinder structure is added between the piezoelectric actuator and the DLPH to eliminate the bending moment acting on the piezoelectric actuator. Through this kind of configuration, the piezoelectric actuator directly drives the moving platform and thus the dynamic performance of the flexure-based mechanism can be improved. In order to adjust the preload for the piezoelectric actuator, a bolt with fine screw mounted behind the piezoelectric actuator is utilized to provide the required preload. The flexure-based mechanism is monolithically manufactured using WEDM technology, and the symmetric configuration of the DLPHs and DCHLs can enhance the decoupling capability of the developed flexure-based mechanism.

Besides the hysteresis phenomenon of piezoelectric actuator, the coupling error is another source of the tracking error, so the platform in this paper is decoupled in structure design. As shown in Fig. 2 (a), a single DCHL can be simplified as a rigid-revolute joint mechanism, it generates a coupling displacement e under the action of force F. Double DCHLs are used in Fig. 2 (b), though the degree of freedom of the mechanism is zero, due to the flexibility of the flexure hinge the middle rigid can still produce a small displacement, and the cross coupling is restrained by the symmetric links, thereby realizing decoupling function. Based on the second mechanism the micro positioning stage is proposed, and the schematic plot of decoupling in the x and y directions is shown in Figs. 2 (c) and (d), respectively, which clearly displays the decoupling property of the

moving stage.

Compared with the previous flexure-based mechanism, the newly designed stage has following advantages. Under the requirement of three dimensional motions and the decoupling, the platform in this paper still keeps an extremely simple structure, which is very rewarding in the machining of prototype. What's more, due to there isn't a displacement amplifier in the proposed mechanism, the stage has a high resonant frequency, which improves the static and dynamic property of the stage greatly, so it is completely competent in the small stroke motion.

3. Theoretical analysis

3.1. Stiffness modeling

Unlike traditional revolute hinge, the flexure hinges have rotational stiffness during the rotation process about the rotational center. This stiffness can affect the static and dynamic characteristics of the flexure-based mechanism in terms of output displacement and natural frequency. Thus, it is necessary to establish the stiffness model of the flexure-based mechanism. There are a number of research efforts dedicated to the stiffness modelling of flexure hinges. The PRBM (pseudo-rigid-body model) method [25] is one of the effective approaches to model the stiffness of flexure-based mechanism. Based on the PRBM technique, the stiffness of the DLPH and DCHL can be given as follows [26]:

$$k_{\mathrm{DLPH}} = \frac{10.72Edt_1^3}{2.55L_1^3} \tag{1}$$

$$k_{\mathrm{DCHL}} = EdR^2 \Bigg/ \left\{ 12 \left[\frac{2s^3\left(6s^2+4s+1\right)}{\left(2s+1\right)\left(4s+1\right)^2} + \frac{12s^4\left(2s+1\right)}{\left(4s+1\right)^{\frac{5}{2}}} \right] \arctan\sqrt{4s+1} \right\} \tag{2}$$

where $s=R/t_2$.

Thus, based on the Lagrange's equation of motion, the stiffness matrix of the flexure-based mechanism can be obtained as follows:

$$K = \mathrm{diag}\left(K_x \quad K_y \quad K_{\theta z}\right) = \mathrm{diag}\left(4k_{DLPH} + \frac{4k_{\mathrm{DCHL}}}{L_2^2} \quad 2k_{DLPH} + \frac{2k_{\mathrm{DCHL}}}{L_2^2} \quad 4a^2k_{DLPH} + \frac{4a^2k_{\mathrm{DCHL}}}{L_2^2} + \frac{8b^2k_{\mathrm{DCHL}}}{L_2^2} \right) \tag{3}$$

where d is the thickness of the flexure hinges, E is the Young's modulus of the material, L_1, L_2, t_1, t_2, R, a, b are defined in Fig. 1.

The stiffness of the piezoelectric actuator and Hertzian contact can be considered as a spring with stiffness k_{pzt} and k_{c}, respectively. In order to guarantee the perfect contact condition between the piezoelectric actuator and the driving point, suitable preload displacement is necessary to avoid the detachment during fast motion of the moving platform. Assume δ_x and δ_y are the initial displacement in the x and y directions, respectively. As shown in Fig. 3, under the action of preload the relative position of the moving platform and two equivalent springs change from the dotted line to the solid line. The stiffness of the flexure-based mechanism with piezoelectric actuators in the x and y directions can be obtained based on the static force analysis. The rational stiffness $K'_{\theta z}$ is given as follows:

$$K'_{\theta z} = K_{\theta z} + \frac{k_{\mathrm{pzt}} k_{\mathrm{cx}}}{k_{\mathrm{pzt}} + k_{\mathrm{cx}}} (a + \delta_y)^2 + \frac{k_{\mathrm{pzt}} k_{\mathrm{cx}}}{k_{\mathrm{pzt}} + k_{\mathrm{cx}}} \left(a - \delta_y\right)^2 + \frac{k_{\mathrm{pzt}} k_{\mathrm{cy}}}{k_{\mathrm{pzt}} + k_{\mathrm{cy}}} \delta_x^2 . \tag{4}$$

Since the initial preload displacement δ_y and δ_x are small enough to be neglected compare with size a, and thus the stiffness of the flexure-based mechanism with actuators in three directions can be written as follows:

$$\begin{cases} K'_x = K_x + \dfrac{2k_{\mathrm{pzt}} k_{\mathrm{cx}}}{k_{\mathrm{pzt}} + k_{\mathrm{cx}}} \\ K'_y = K_y + \dfrac{k_{\mathrm{pzt}} k_{\mathrm{cy}}}{k_{\mathrm{pzt}} + k_{\mathrm{cy}}} \\ K'_{\theta z} = K_{\theta z} + \dfrac{2a^2 k_{\mathrm{pzt}} k_{\mathrm{cx}}}{k_{\mathrm{pzt}} + k_{\mathrm{cx}}} \end{cases} \tag{5}$$

3.2. Stress analyses

In order to guarantee the repeatability and durability of the flexure-based mechanism, the stress of flexure hinges must be examine to maintain the maximum stress less than the allowable stress of material. Due to the different geometric structures, the maximum stress of the flexure-based mechanism mainly occurs at the root of the leaf parallelogram and the thinnest part of the right circular hinge. Thus, it is necessary to calculate the stress in these sections. Since the rotational motion of the developed flexure-based mechanism has no effect on the deformation of DLPH due to the decoupling characteristics of the DCHL, and thus the maximum stress of DLPH can be obtained as follows [27]:

$$\sigma_{\mathrm{maxDLPH}} = \frac{3k_{b1} \Delta E t_1}{L_1^2} \tag{6}$$

where Δ is the axial maximum displacement of DLPH, k_{b1} is stress concentrate coefficient.

The maximum stress of right circular hinge occurs at the surface of the minimal thickness, which can be obtained according to the knowledge of Material Mechanics

$$\sigma_{\max \mathrm{DCH}L}=\frac{6k_{b2}k_{\mathrm{DCH}L}\left(\max\left\{\Delta x,\Delta y\right\}+a\Delta\alpha\right)\Delta Et_1}{dt_2^2L_2} \tag{7}$$

where Δx, Δy, $\Delta\alpha$ are displacement in three directions, k_{b2} is stress concentrate coefficient.

3.3. Workspace analyses

The workspace of the flexure-based mechanism is mainly determined by the allowable stress limitation of the material and the maximum stroke of the piezoelectric actuator. The intersection of these two constrained space is defined as the reachable workspace. In order to obtain the maximum reachable workspace, the maximum stress of the flexure hinges is within the allowable stress during the motion of the moving platform, which can be guaranteed during the mechanical design and optimization. This is to say that the workspace of the flexure-based mechanism is determined by the maximum stroke of the piezoelectric actuators. Due to the rotational stiffness of the flexure hinges and the compliance of the piezoelectric actuator, the output displacement of moving platform will be less than the nominal displacement of the actuator. With consideration of the contact stiffness, the relationship between the displacement of piezoelectric actuator and the output of the moving platform can be given as follows

$$\mathrm{S}_{\mathrm{apzt}}=\frac{k_{\mathrm{pzt}}\left(k_{\mathrm{c}}+K\right)}{k_{\mathrm{pzt}}\left(k_{\mathrm{c}}+K\right)+k_{\mathrm{c}}K}S_{\mathrm{npzt}} \tag{8}$$

where S_{apzt} and S_{npzt} are the actual and nominal output displacement of the piezoelectric actuator, respectively.

Based on the kinematics relationship between the piezoelectric actuators and the moving platform, the workspace of the flexure-based mechanism can be obtained. Due to the orthogonal configuration and decoupling characteristics, the displacement in x and y directions is equal to the actual output of piezoelectric actuators. The maximum rotational angle is determined by the actual displacement of the piezoelectric actuator and the distance between the two actuation points in the x direction.

$$\begin{cases} x=\left(S_{\mathrm{apzt2}}+S_{\mathrm{apzt3}}\right)/2 \\ y=S_{\mathrm{apzt1}} \\ \theta_z=\left(S_{\mathrm{apzt2}}-S_{\mathrm{apzt3}}\right)/2a \end{cases} \qquad 0\le S_{\mathrm{apzt}i}\left(i=1,2,3\right)\le S_{a\max} \tag{9}$$

where S_{apzti} is the actual output displacement of the ith piezoelectric actuator, and S_{amax} is the actual maximum output of the piezoelectric.

3.4. Dynamic modeling

From dynamics point of view, the piezoelectric actuator and flexure-based mechanism can be considered as the lumped mass spring system. With consideration of the contact stiffness and damping ratio, the dynamic model of the developed flexure-based mechanism is show in Fig. 4. Due to the decoupling characteristics of the mechanism, the dynamic models in y direction and in the x and θ_z directions are shown in Figs. 4(a) and (b) respectively. In the model, c_{pzt}, m_{pzt} and k_{pzt} are the damping ratio, mass and equivalent stiffness of piezoelectric actuator, respectively; m and J are the mass and rotational inertia of the working platform, respectively; damping ratios of the flexure-based mechanism in the x, y, and θ_z directions are c_x, c_y, $c_{\theta z}$, respectively. The equivalent stiffness and damping ratio of the Hertzian contact are k_c and c_c, respectively. Both x_{pzt} and y_{pzt} denote the extension of the piezoelectric actuator, x_m, y_m, θ_z are the displacements and rotation angle of moving platform. The force generated by piezoelectric actuator is denoted by F_{pzti} (i=1, 2, 3).

Based on the Newton second motion law, the dynamic model of the developed flexure-based mechanism can be given as follows:

$$\begin{bmatrix} m_{pzt} & 0 \\ 0 & m \end{bmatrix}\begin{bmatrix} \ddot{y}_{pzt} \\ \ddot{y}_m \end{bmatrix}+\begin{bmatrix} c_c+c_{pzt} & -c_c \\ -c_c & c_c+c_y \end{bmatrix}\begin{bmatrix} \dot{y}_{pzt} \\ \dot{y}_m \end{bmatrix}+\begin{bmatrix} k_c+k_{pzt} & -k_c \\ -k_c & k_c+K_y \end{bmatrix}\begin{bmatrix} y_{pzt} \\ y_m \end{bmatrix}=\begin{bmatrix} F_{pzt1} \\ 0 \end{bmatrix}. \tag{10}$$

$$\begin{bmatrix} m_{pzt} & 0 & 0 & 0 \\ 0 & m_{pzt} & 0 & 0 \\ 0 & 0 & m & 0 \\ 0 & 0 & 0 & J \end{bmatrix}\begin{bmatrix} \ddot{x}_{pzt1} \\ \ddot{x}_{pzt2} \\ \ddot{x}_m \\ \ddot{\theta}_z \end{bmatrix}+\begin{bmatrix} c_c+c_{pzt} & 0 & -\frac{c_c}{2} & \frac{c_c a}{2} \\ 0 & c_c+c_{pzt} & -\frac{c_c}{2} & -\frac{c_c a}{2} \\ -c_c & -c_c & 2c_c+c_x & 0 \\ c_c a & -c_c a & 0 & 2c_c a^2+c_{\theta z} \end{bmatrix}\begin{bmatrix} \dot{x}_{pzt1} \\ \dot{x}_{pzt2} \\ \dot{x}_m \\ \dot{\theta}_z \end{bmatrix}+\begin{bmatrix} k_c+k_{pzt} & 0 & -\frac{k_c}{2} & \frac{k_c a}{2} \\ 0 & k_c+k_{pzt} & -\frac{k_c}{2} & -\frac{k_c a}{2} \\ -k_c & -k_c & 2k_c+K_x & 0 \\ k_c a & -k_c a & 0 & 2k_c a^2+K_{\theta z} \end{bmatrix}\begin{bmatrix} x_{pzt1} \\ x_{pzt2} \\ x_m \\ \theta_z \end{bmatrix}=\begin{bmatrix} F_{pzt2} \\ F_{pzt3} \\ 0 \\ 0 \end{bmatrix} \tag{11}$$

In order to investigate the relationship between inputs and outputs of the flexure-based mechanism, the transfer function should be provided to conduct the performance analysis in frequency domain. For simplicity and without loss generality, the transfer function in y direction is developed. Define the state vector $\mathbf{Y}=\begin{bmatrix} y_{pzt} & \dot{y}_{pzt} & y_m & \dot{y}_m \end{bmatrix}^{\mathrm{T}}$, $y=\begin{bmatrix} y_{pzt}, y_m \end{bmatrix}^T$, and thus the state space function of the flexure-based mechanism in y direction can be given as follows:

$$\begin{cases} \dot{\boldsymbol{Y}}=A_y\boldsymbol{Y}+B_y F_{pzt1} \\ y=C_y\boldsymbol{Y} \end{cases}. \tag{12}$$

where $A_y = \begin{bmatrix} 0 & 1 & 0 & 0 \\ -\dfrac{k_c + k_{pzt}}{m_{pzt}} & -\dfrac{c_c + c_{pzt}}{m_{pzt}} & \dfrac{k_c}{m_{pzt}} & \dfrac{c_c}{m_{pzt}} \\ 0 & 0 & 0 & 1 \\ \dfrac{k_c}{m} & \dfrac{c_c}{m} & -\dfrac{k_c + K_y}{m} & -\dfrac{c_c + c_y}{m} \end{bmatrix}$, $B_y = \begin{bmatrix} 0 & \dfrac{1}{m_{pzt}} & 0 & 0 \end{bmatrix}^T$, $C_y = \begin{bmatrix} 1 & 0 & 0 & 0 \\ 0 & 0 & 1 & 0 \end{bmatrix}$.

Accordingly, the transfer function of the flexure-based mechanism in the y direction can be obtained:

$$G_y(s) = C_y(sI - A_y)^{-1} B_y . \tag{13}$$

Similarly, the transfer functions in the x and θ_Z directions can be given as follows:

$$G_{x\theta z}(s) = C_{x\theta z}(sI - A_{x\theta z})^{-1} B_{x\theta z} \tag{14}$$

where $A_{x\theta z} = \begin{bmatrix} 0 & 1 & 0 & 0 & 0 & 0 & 0 & 0 \\ -\dfrac{k_c + k_{pzt}}{m_{pzt}} & -\dfrac{c_c + c_{pzt}}{m_{pzt}} & 0 & 0 & \dfrac{k_c}{2m_{pzt}} & \dfrac{c_c}{2m_{pzt}} & -\dfrac{k_c a}{2m_{pzt}} & -\dfrac{c_c a}{2m_{pzt}} \\ 0 & 0 & 0 & 1 & 0 & 0 & 0 & 0 \\ 0 & 0 & -\dfrac{k_c + k_{pzt}}{m_{pzt}} & -\dfrac{c_c + c_{pzt}}{m_{pzt}} & \dfrac{k_c}{2m_{pzt}} & \dfrac{c_c}{2m_{pzt}} & \dfrac{k_c a}{2m_{pzt}} & \dfrac{c_c a}{2m_{pzt}} \\ 0 & 0 & 0 & 0 & 0 & 1 & 0 & 0 \\ \dfrac{k_c}{m} & \dfrac{c_c}{m} & \dfrac{k_c}{m} & \dfrac{c_c}{m} & -\dfrac{2k_c + K_x}{m} & -\dfrac{2c_c + c_x}{m} & 0 & 0 \\ 0 & 0 & 0 & 0 & 0 & 0 & 0 & 1 \\ -\dfrac{k_c a}{J} & -\dfrac{c_c a}{J} & \dfrac{k_c a}{J} & \dfrac{c_c a}{J} & 0 & 0 & -\dfrac{2k_c a^2 + K_{\theta z}}{J} & -\dfrac{2c_c a^2 + c_{\theta z}}{J} \end{bmatrix}$,

$B_{x\theta z} = \begin{bmatrix} 0 & \dfrac{1}{m_1} & 0 & 0 & 0 & 0 & 0 & 0 \\ 0 & 0 & 0 & \dfrac{1}{m_1} & 0 & 0 & 0 & 0 \end{bmatrix}^T$, $C_{x\theta z} = \begin{bmatrix} 1 & 0 & 0 & 0 & 0 & 0 & 0 & 0 \\ 0 & 0 & 1 & 0 & 0 & 0 & 0 & 0 \\ 0 & 0 & 0 & 0 & 1 & 0 & 0 & 0 \\ 0 & 0 & 0 & 0 & 0 & 0 & 1 & 0 \end{bmatrix}$.

4. Optimization design and simulation verification

According to the above analyses, it is noted that the geometric parameters have significant influences on the performance of the flexure-based mechanism, and thus it is crucial to conduct the mechanical design optimization to improve the static and dynamic characteristics of the developed flexure-based mechanism. In order to increase the bandwidth of the entire system, the first natural frequency of the flexure-based mechanism should be large enough to improve the dynamic characteristics. Thus, the first natural frequency is chosen as the objective function to optimize the parameters of the flexure-based mechanism. The constraint conditions of the optimization are given as follows:

1) Maximum stress: as mentioned previously, the maximum stresses occur at the root of DLPH and/or the minimal thickness of the DCHL. Both of the maximum stresses should be lower than the

allowable stress of material. Considering the positioning accuracy repeatability and durability, the stress concentration coefficients are chosen as k_{b1}=1.5, k_{b2}=1.3 for DLPH, and DCHL, respectively. Thus, the stress constrain can be expressed as follows:

$$\begin{cases} \sigma_{\text{maxDLPH}} \le \sigma_{\text{m}} / s_f \\ \sigma_{\text{maxDCHL}} \le \sigma_{\text{m}} / s_f \end{cases} \tag{15}$$

where σ_{m} is yield strength, and σ_{m}=400 MPa, s_f is the safety factor and chosen as 2.5.

2) Stiffness of the flexure-based mechanism: the relationship between the actual and nominal output has been displayed in Eq. (8), and it can be transformed into the following formula:

$$\text{S}_{\text{max}} = \frac{k_{\text{pzt}}}{k_{\text{pzt}} + k_{\text{c}}\left(\dfrac{1}{1+\text{k}_c / K}\right)} S_{\text{pzt}} \tag{16}$$

Eq. (15) indicates the reduce of the stiffness of the mechanism K can lead to a longer output of the platform, so in order to obtain big enough stroke of the moving platform, it is better to limit the stiffness of the flexure-based mechanism into a proper range:

$$K_x \le 0.1 k_{\text{pzt}}, \quad K_y \le 0.1 k_{\text{pzt}} \tag{17}$$

3) Machining accuracy and stability: The stiffness of DCHL is calculated by Eq. (2), and to guarantee the calculation accuracy and the material buckling of the DCHL, it is feasible to choose $0.05 \le t_2 / R \le 0.65$. In the design of the DLPH, the stiffness of the DLPH is computed based on the PRBM (pseudo-rigid-body) model technique, a higher ratio t_1/L_1 cuts down the modeling accuracy of DLPH, so it is better to select $L_1 \ge 15 t_1$.

The flexure-based mechanism is manufactured by WEDM technology, which has a minimum machining thickness to ensure a high accuracy, so considering the structural compactness and machining feasibility of the flexure-based mechanism, the ranges of the variables are chosen as follows: $0.3 \le t_1 \le 1$, $0.3 \le t_2 \le 1$, $5 \le L_1 \le 30$, $5 \le L_2 \le 30$, $1 \le R \le 3$. The optimization process is conducted using Matlab code, and the optimization results are shown in Table 1. The natural frequencies of the optimized flexure-based mechanism are f_x=574.84 Hz, f_y=466.6 Hz, $f_{\theta z}$=516 Hz.

Based on the established model, the reachable workspace of the developed flexure-based mechanism can be calculated. The nominal maximum stroke of the piezoelectric actuator is 15 μm. According to Eq. (8) and (9), the workspace of the developed flexure-based mechanism is shown in Fig. 5. It is noted that the working range in the y direction is independent with the x direction, and

the maximal displacement of the moving platform in the x and y directions are respectively 14.3 μm and 14.5 μm when the rotational angle is equal to zero. The rotational angle range of the moving platform is $\pm 0.0136°$. The stroke in the x direction decreases with the increasing rotational angle. However, the stroke in y direction is not affected by the rotational angle.

Since the Hertzian contact have significant influences on the dynamic performance of the flexure-based mechanism, it is necessary to obtain further insights into the contact stiffness between the piezoelectric actuator and the moving platform. For simplicity and without loss generality, the dynamic performance of the moving platform in the y direction is analyzed. Based on Eq. (13) and obtained geometric and physical parameters, the Bode plat of the developed mechanism with different contact stiffness is shown in Fig. 6, where the blue solid line represents the transfer function from $F_{\mathrm{pzt1}}$to y_{pzt}, and the green dash line represents the transfer function from F_{pzt1} to y_{m}. It is noted that 1) both the magnitude remains constant in low frequency, and the magnitude from F_{pzt1} to y_{pzt} is lager than that from F_{pzt1} to y_{m}, which means the displacement of the piezoelectric actuator and the moving platform are linear to the force in low frequency, but output displacement of the moving platform is less than that of the piezoelectric actuator. 2) The magnitude from F_{pzt1} to y_{pzt} and from F_{pzt1} to y_{m} is tending to be equivalent as the contact stiffness increase. 3) The resonant frequency becomes larger when contact stiffness increases. These phenomena indicate high contact stiffness can improve the performance of the flexure-based mechanism.

To better understand the influence of the contact stiffness to the system, the relationship between contact stiffness and the magnitude ratio (the ration of magnitude from F_{pzt1} to y_{pzt} and magnitude F_{pzt1} to y_{m}) is shown in Fig. 7. It is noted that the contact stiffness has an significant influence on the magnitude ratio in the small contact stiffness range, but the influence becomes very small when it exceed a certain constant, which indicates the contact stiffness should be chosen in an appropriate value, and thus the output displacement of the platform and piezoelectric actuator tend to be same.

In order to validate the established modes, FEA is conducted using ANSYS software to estimate the stiffness and the natural frequency of the flexure-based mechanism. The finite element type is chosen as SOLID 185. For the Aluminum Alloy T7075, the Young's modulus is chosen E=71 GPa, density ρ=2770kg/m^3, and Poisson's ratio ν=0.33.

Table 2 lists the stiffness and natural frequencies of the flexure-based mechanism without actuators using FEA and experimental testing, as well as theoretical analyses. It is noted that the

results are in good agreement with each other, and indicating that the correctness of the established models. In the FEA of the flexure-based mechanism with piezoelectric actuator, the piezoelectric is considered as a spring with a constant stiffness k_{pzt}, one end of the spring is fixed and the other end is attached on DLPH. Figs. 8 and 9 show the first three mode shapes of the flexure-based mechanism with and without piezoelectric actuators, respectively. The first three natural frequencies with piezoelectric actuators are 837.70HZ, 620.08HZ, 731.25 HZ in the x, y and θ_Z directions, respectively, It is noted that the piezoelectric actuators can significantly improve the natural frequencies of the flexure-based mechanism, but they don't change the mode shape.

5. EXPERIMENTS

5.1. Controller design

In order to eliminate the hysteresis of piezoelectric actuators, the hybrid feedforward/feedback controller is developed and constructed. The feedforward controller is in a novel form compared with the previous research. The rate-dependent PI hysteresis model is utilized, and the structure of the PI hysteresis model consists of backlash and dead zone operators in serial connection, as well as the cubic polynomial function in parallel connection. This kind of configuration can improve the control accuracy and reduce the complexity of the controller. Further, the direct parameter identification for the inverse PI hysteresis model is conducted to avoid the complex inversion computation of the rate-dependent PI hysteresis model. The modified inverse PI model is defined as follows:

$$u(t)=\Gamma^{-1}(y,\dot{y})=G(y)+\vec{w}_h{}^T\vec{H}_r\left[\vec{w}_s(\dot{y})^T\cdot\vec{S}_d[y](t)\right] \tag{18}$$

where y is the desired trajectory, u is the output of the model and also the voltage sent to piezoelectric actuator, H, S is a superposition of backlash operators and dead-zone operators respectively, w_h, w_s is the slope of a backlash operator and dead-zone operator, respectively, G is a cubic polynomial input function, which is multiplied with the backlash and dead-zone operators.

$$\vec{w}_h{}^T=\left[w_{h1},w_{h2},w_{h3},\cdots w_{hn}\right]^T,\ \vec{H}_r[y](t)=\left[H_{r1}[y](t),H_{r2}[y](t),\cdots H_{rn}[y](t)\right]^T,$$

$$\vec{w}_s{}^T=\left[w_{s1},w_{s2},w_{s3},\cdots w_{sn}\right]^T,\ \vec{S}_d[y](t)=\left[S_{d1}[y](t),S_{d2}[y](t),\cdots S_{dn}[y](t)\right]^T,$$

$$w_{hi}=k_i\dot{y}(t)+b_i,\ G(y)=a_1y(t)^3+a_2y(t)^2+a_3y(t)+a_4. \tag{19}$$

The inverse model has ten backlash operators and six dead-zone operators [28], and the parameter identification is implemented by ‘lscurvefit’ function in MATLAB environment.

The feedback controller is a traditional Proportional-Integral (PI) controller, which is used to compensate the uncertainty from environment, and feedforward controller eliminates most of the hysteresis. The block diagram of the hybrid feedforward/feedback control is illustrated in Fig. 10.

5.2. Experiment testing

In order to examine the established mechanical design and control methodologies, a prototype of the flexure-based mechanism is monolithically developed. The WEDM technique is utilized to manufacture the flexure-based mechanism. The aluminum alloy T7075 is chosen for the excellent physical and thermal properties. In order to reduce the external disturbance effects on the testing system, the flexure-based mechanism is mounted on a Newport RS-4000 optical table. The stiffness testing setup is shown in Fig. 11. A pull-push force gauge (NK-20) is utilized to provide the require load on the moving platform, and a displacement sensor indicator (TESA 04430011) is used to record the corresponding displacement of the moving platform. Based on the Hook's law, the experimental stiffness is listed in Table 2. As mentioned previously, the experimental results are in good agreement with those of FEA and theoretical analyses.

Fig. 12(a) shows the experiment setup for the modal analysis. The impact modal analyzer is utilized to obtain the FRF (Frequency Response Function) of the flexure-based mechanism. A hammer (IH-05) with force gauge is utilized to implement impact force on the moving platform, and an accelerometer (Brüel&kjær, 4366) is used to pick up the acceleration response of the moving platform. The force and acceleration signals are supplied to the dynamic analyzer (TST5912) to obtain the FRF of the developed flexure-based mechanism. Fig. 12(b) shows the FRF of the flexure-based mechanism without actuators, and the corresponding frequencies are listed in Table 2, it is noted that the experiment results are smaller than the analytical and FEM results, this is mainly caused by the additional mass of the acceleration sensor and the bracket on the moving platform. When the piezoelectric actuators are installed on the flexure-based mechanism and initial preload is applied. The FRF of the developed flexure-based mechanism is shown in Fig. 12(c). The corresponding nature frequencies are 1130 Hz, 970 Hz, 790 Hz in the x, y, θ_Z directions, respectively. Natural frequencies increase in all three directions due to the stiffness of the piezoelectric actuators, which is in good agreement with the analytical results.

The control system of the flexure-based mechanism is shown in Fig. 13. Three piezoelectric actuators (THORlabs AE0505D18F) are employed to drive the moving platform. The nominal

maximal displacement of such kinds of actuators is 15 μm in 100V. The piezoelectric actuator is driven by a PI E-505.00 piezoelectric amplifier, which has a constant amplification factor 10. Laser displacement sensor (KEYENCE LK-H050) is utilized to measure the displacement of the moving platform to form closed loop control. A dSPACE DS1103 R&D control board is utilized to provide a real-time control at a sampling rate of 5 KHz.

The output displacement of the flexure-based mechanism is measured under open loop condition, and shown in Fig. 14. It can be seen that the maximum displacement in x and y directions is 12.74 μm and 12.22 μm, respectively. The slightly difference between the two axes is mainly due to the assembly and manufacture errors. The maximum rotational angles of the moving platform in clockwise and anti-clockwise are 0.0088° and 0.0103°, respectively. The reason for the difference is the different preload and assembly errors. However, it is noted that the experimental results are less than those of theoretical analyses. This is caused by the stiffness of the flexure-based mechanism which reduced the output displacement of the moving platform compared with the nominal displacement of piezoelectric actuator. It is also obvious that there are hysteresis phenomena in the motion of the moving platform. Thus, it is crucial to reduce this kind of hysteresis and improve the positioning accuracy of the flexure-based mechanism for the practical applications.

Based on the proposed hybrid feedforward/feedback controller, a series of experiments are implemented to verify the performance and effectiveness of the developed control methodology. The trajectory tracking of a single sinusoidal input signal in x and y directions are shown in Figs. 15 and 16, respectively. It is noted that the feedforward controller based on the hybrid inverse PI hysteresis model can reduce the hysteresis of the moving platform to some extent, and the moving platform can follow the input signal very well. The maximum error is 0.1241 μm, and the root mean square (RMS) error is 0.03701 μm in x direction as shown in Fig. 15(a). However, the combined feedforward/feedback controller can further improve the tracking capability of the flexure-based mechanism as shown in Fig. 15 (b), where the maximal tracking error is 0.0869 μm and the RMS error is 0.02473 μm. The same results can be seen in the trajectory tracking capability of the moving platform in y direction as shown in Fig. 16. The reason is mainly due to the time varying nonlinear hysteresis of the piezoelectric actuator. The developed feedforward controller can not totally eliminate the nonlinearity of the flexure-based mechanism, which can be reduced by the closed loop control method. Thus, the combination of the feedforward and feedback controller is the best choice for such kinds of flexure-based mechanisms. As shown in Figs. 15(c) and 16(c), the

coupling error in each axis is also measured during signal tracking, note that the coupling errors in the *x* direction is measured by sensors s_2 and s_3 simultaneously. According to the experimental data, the function of the decoupling mechanism is limited regardless the theoretical correctness, the main reason maybe the machining errors and assembly errors, or the uncertain preload of piezoelectric actuators in the *x* direction, so in order to better control the motion of the stage it's worthy for deeper research on decoupling control method.

Further another sinusoidal signal with a higher frequency 10 Hz in the *y* direction is tracked to verify the correctness of the modeling method, after the parameter identification with a high-frequency input signal, the tracking results with feedforward and feedforward/feedback controller are shown in Fig. 17, which indicate the proposed hysteresis model can also be used in tracking a high-frequency signal, but the tracking error has a little increase. Besides the common motion in the *x* and *y* directions, the rotation about the *z* axis can also be realized in the newly-designed mechanism, Fig. 18 is a simple tracking on a rotation signal with the feedforward/feedback controller and the maximal error is about 1.5% of the stroke, manifesting the high tracking precision.

6. Conclusions

The mechanical design and control methodology of a compact and simple 3-DOF (X-Y-θ_Z) planar flexure-based mechanism has been developed. The stage adopts two different kinds of flexure hinges，DCHL and DLPH, to realize the 3-D motion and the decoupling mechanism. The prototype with a dimension 170×170×18 mm^3 has been manufactured. The natural frequencies of the flexure-based mechanism in the experimental testing are 1130 Hz, 970 Hz, 790 Hz in the x, y, θ_Z directions, and the open loop maximum displacements in *x* and *y* direction are 12.74 μm, 12.22 μm, respectively. The maximal rotation angle in clockwise and anticlockwise is 0.0088° and 0.0103°, respectively.

The static and dynamic models of the developed flexure-based mechanism have been developed based on the spring mass model methodology. The mechanical design optimization has been performed to improve the performance of the flexure-based mechanism. The influence of the contact stiffness on the dynamic performance of the flexure-based mechanism has been studied. FEA is utilized to examine the theoretical analyses. A novel combined feedforward/feedback control methodology has been proposed to eliminate the nonlinear hysteresis and to reduce external disturbance of the flexure-based mechanism. A number of experimental testing has been conducted

to verify the dynamic performance of the developed flexure-based mechanism. The research achievements provide guides for such kinds of compact flexure-based mechanism design.

Acknowledgement

This research is supported by National Natural Science Foundation of China (Nos. 51275337, 51175372), National Key Special Project of Science and Technology of China (No. 2011ZX04016-011), Reserved Academic Program of Peiyang Scholar, and Program for New Century Excellent Talents in University (No. NCET-11-0374).

References

[1] Y. Li, J. Huang, and H. Tang, “A compliant parallel XY micro motion stage with complete kinematic decoupling,” IEEE Transactions on Automation Science and Engineering, vol. 9, no. 12, pp. 538-553, 2012.

[2] B. A. Gozen, O. B. Ozdoganlar, “Design and evaluation of a mechanical nanomanufacturing system for nanomilling,” Precision Engineering, vol. 36, no. 1, pp. 19-30, 2012.

[3] Y. Yan, Z. Hu, X. Zhao, T. Sun, “Top-down nanomechanical machining of three-dimensional nanostructures by atomic force microscopy,” Small, vol. 6, no. 6, pp. 724-728, 2010.

[4] S. Thalhammer, “Laser micro-tools in cell biology and molecular medicine,” Laser Physics, vol. 13, no. 5, pp. 681-691, 2003.

[5] N. Bonnail. “Variable structure of a piezoelectric actuator for a scanning tunneling microscope,” IEEE Transaction on Industrial Eletronics, vol. 51, no. 2, pp. 354-363, 2004.

[6] Y. Zhao, F. Gao, X. Dong, X. Zhao, "Dynamics analysis and characteristics of the 8-PSS flexible redundant parallel manipulator", Robotics and Computer-Integrated Manufacturing, vol. 27, no. 5, pp. 918-928, 2011.

[7] Y. Qin, Y. Tian, D. Zhang, B. Shirinzadeh, S. Fatikow, “A novel direct inverse modeling approach for hysteresis compensation of piezoelectric actuator in feedforward applications,” IEEE/ASME Transactions of Mechatronics, vol. 18, no. 3, pp. 981-989, 2013.

[8] Y. Tian, D. Zhang, B. Shirinzadeh, “Dynamic modelling of a flexure-based mechanism for ultra precision grinding operation,” Precision Engineering, vol. 35, no. 4, pp. 554-565, 2011.

[9] Y. Tian, Z. Guo, F. Wang, J. Li, D. Zhang, B. Shirinzadeh, “Design and experimental investigation of a 2-DOF planar micro-positioning table,” International Journal of Intelligent Mechatronics and Robotics (IJIMR), vol. 3. no. 2. pp. 39-54, 2013.

[10] F.C.W. Diana, K. Tim, J. Radivoje, “Freeing the serial mechanism designer from inverse kinematic solvability constraints,” Applied Bionics and Biomechanics, vol. 7, no. 3, pp. 209-216, 2010.

[11] L. Lai, G. Gu, and L. Zhu, “Design and control of a decoupled two degree of freedom translational parallel micro-positioning stage,” Review of Scientific Instruments, vol. 83, no. 4, p. 045105, 2012.

[12] Q. Xu, “Design and Development of a Compact Flexure-Based XY Precision Positioning System with Centimeter Range,” IEEE Transactions on Industrial Electronics, vol. 61, no. 2, pp. 893-903, 2013.

[13] Yangmin Li, and Qingsong Xu, "Design and Analysis of a Totally Decoupled Flexure-Based XY Parallel Micromanipulator", IEEE Transactions on Robotics, vol. 25, no. 3, pp. 645-657, 2009.

[14] Q. Yao, J. Dong, P.M. Ferreira, “Design, analysis, fabrication and testing of a parallel-kinematic micropositioning XY stage,” International Journal of Machine Tools & Manufacture, vol. 47, no. 6, pp. 946-961, 2007.

[15] H. Kim and D. Gweon “Development of a compact and long range XYθz nano-positioning stage”, Review of Scientific Instruments, vol. 83, no. 8, p. 085102, 2012.

[16] Y. Tian, B. Shirinzadeh, D. Zhang, “Design and dynamics of a 3-DOF flexure-based parallel mechanism for micro/nano manipulation,” Microelectronic Engineering, vol. 87, no. 2, pp. 230-241, 2010.

[17] H. Kim, D. H. Ahn and D. G. Gweon, “Development of a novel 3-degrees of freedom flexure based positioning system,” Review of Scientific Instruments, vol. 83, no. 5, p. 055114, May 2012.

[18] Y. Qin, B. Shirinzadeh, D. Zhang, Y. Tian, “Design and Kinematics Modeling of a Novel 3-DOF Monolithic Manipulator Featuring Improved Scott-Russell Mechanisms,” Journal of Mechanical Design, vol. 135, no. 10, p. 101004, 2013.

[19] K. Kuhnen, “Modeling, identification and compensation of complex hysteretic nonlinearities: a modified Prandtl-Ishlinskii approach,” Europen Journal of Control, vol. 9, no. 4, pp. 407-418, 2003.

[20] M. A. Janaideh, S. Rakheja, and C.-Y. Su, “An analytical generalized Prandtl-Ishlinskii model inversion for hysteresis compensation in micropositioning control,” IEEE/ASME Trans. Mechatronics, vol. 16, no. 4, pp. 734-744, 2011.

[21] G. Gu, L. Zhu, C. Su, H. Ding, "Motion control of piezoelectric positioning stages: modeling, controller design and experimental evaluation," IEEE/ASME Transactions on Mechatronics, vol. 18, no. 5, pp. 1459-1471, 2013.

[22] G. Gu, L. Zhu, C. Su, "Modeling and compensation of asymmetric hysteresis nonlinearity for piezoceramic actuators with a modified Prandtl-Ishlinskii model," IEEE Transactions on Industrial Electronics, vol. 61, no.3, pp. 1583-1595, 2014.

[23] G. Gu and L. Zhu, “High-speed tracking control of piezoelectric actuators using an ellipse based hysteresis model,” Review of Scientific Instruments, vol. 81, no. 8, p.085104, 2010.

[24] G. Gu, M. Yang, and L. Zhu, “Real-time inverse hysteresis compensation of piezoelectric actuators with a modified Prandtl-Ishlinskii model,” Review of Scientific Instruments, vol. 83, no.6, p.065106, 2012.

[25] A. Midha, L. L. Howell, T. W. Norton, “Limit positions of compliant mechanisms using the pseudo-rigid-body model concept,” Mechanism and Machine Theory, vol. 35, no. 1, pp. 99-115, 2000.

[26] Y. Wu, Y. Zhao, “Design calculations for flexure hinges," Review of Scientific Instruments, vol.73, no. 8, pp. 3101-3106, 2002.

[27] Y. Gao, D. Zhang, C. W. Yu, “Detachment modeling of a novel workpiece micro-positioning table under preloaded hertz contact,” Precision Engineering, vol. 26, no. 1, pp. 83-92, 2002.

[28] W. T. Ang, P. K. Khosla, and C. N. Riviere, “Feedforward controller with Inverse rate-dependent model for piezoelectric actuators in trajectory tracking applications,” IEEE/ASME Trans. Mechatronics, vol. 12, no. 2, pp. 134–142, April 2007.

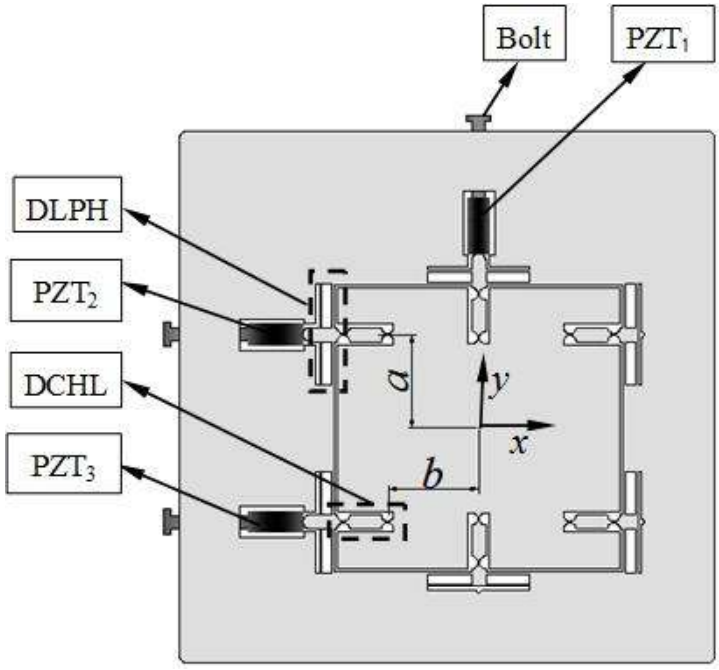

(a) Schematic of the positioning mechanism

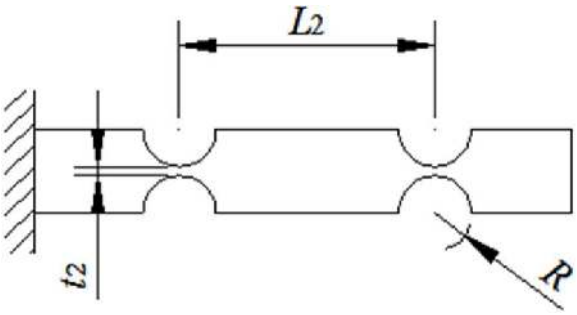

(b) Double circular hinge linkage

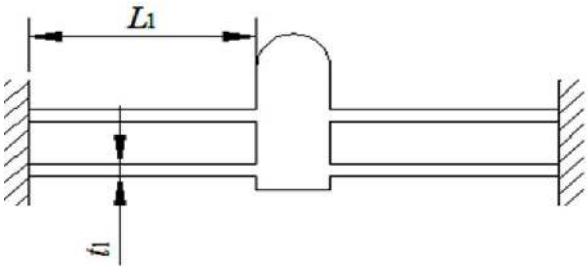

(c) Dual leaf parallelogram hinge

Fig. 1. Developed 3-DOF flexure-based mechanism

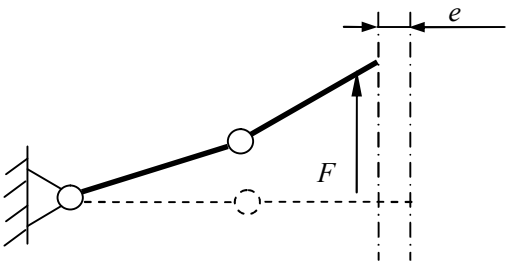

(a) Simplification of DCHL

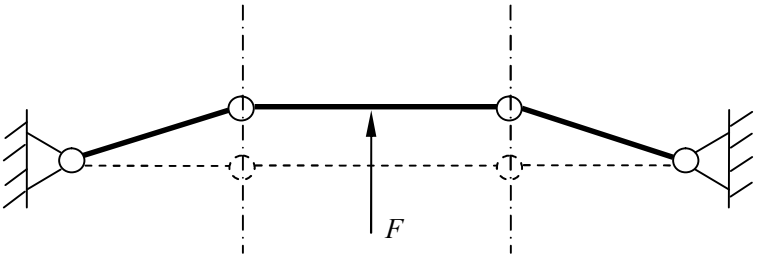

(b) Double DCHL

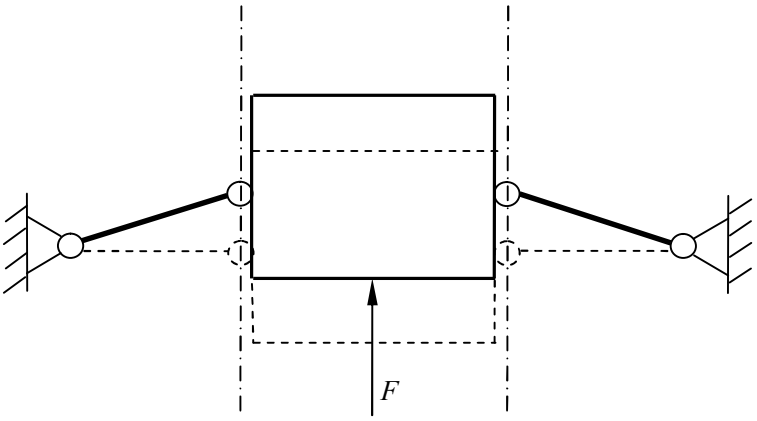

(c) Schematic plot of decoupling in *x* direction

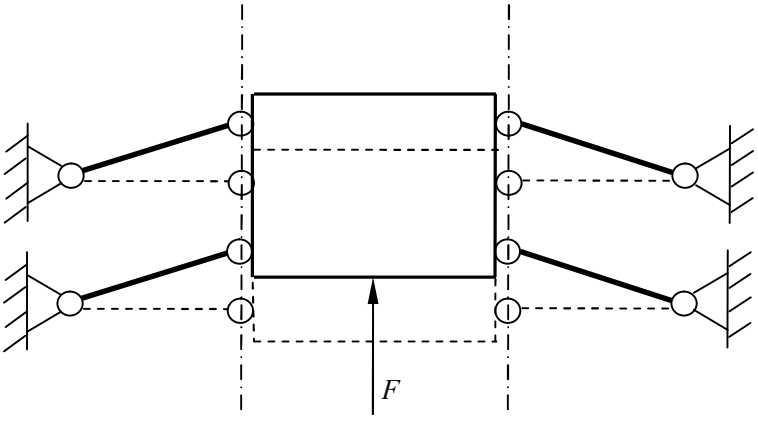

(d) Schematic plot of decoupling in *y* direction

Fig. 2. The decoupling realization in structure design

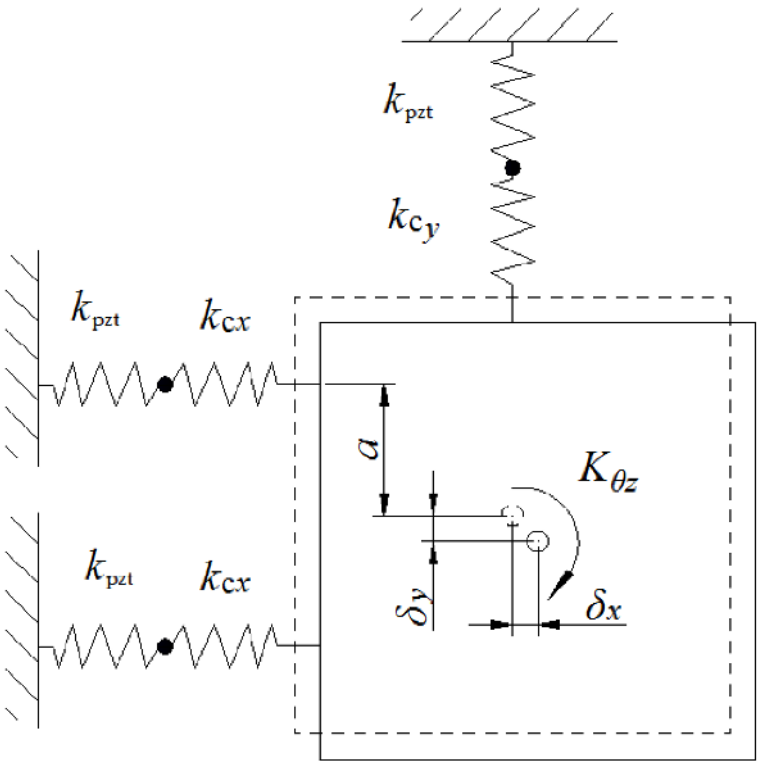

Fig. 3. Stiffness model of the flexure-based mechanism

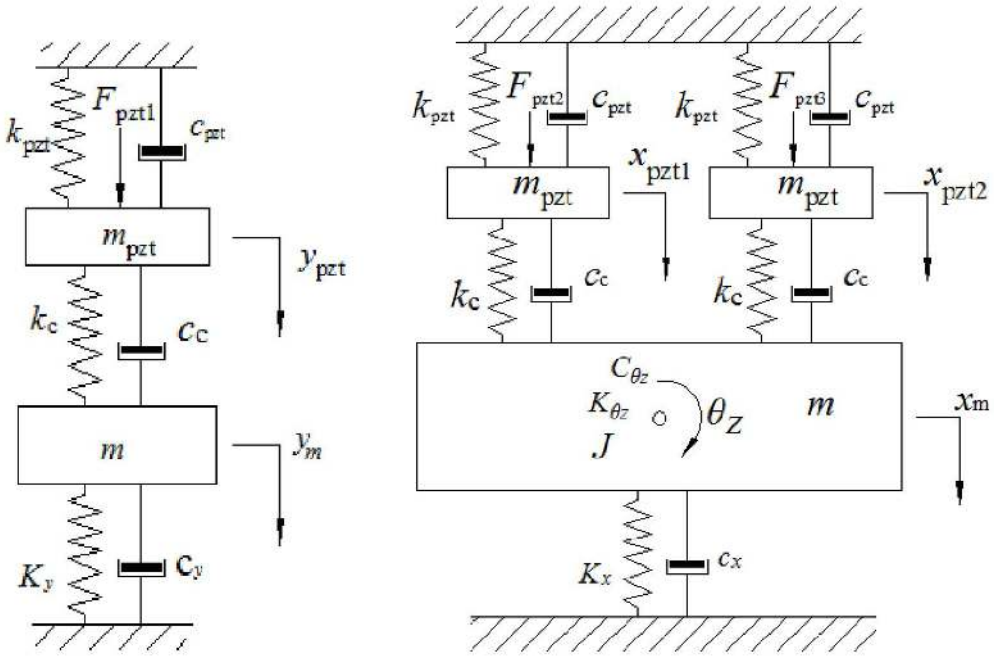

(a) Dynamic model in y direction (b) Dynamic model in x and θ_Z direction

Fig. 4. Dynamic models of the flexure-based mechanism

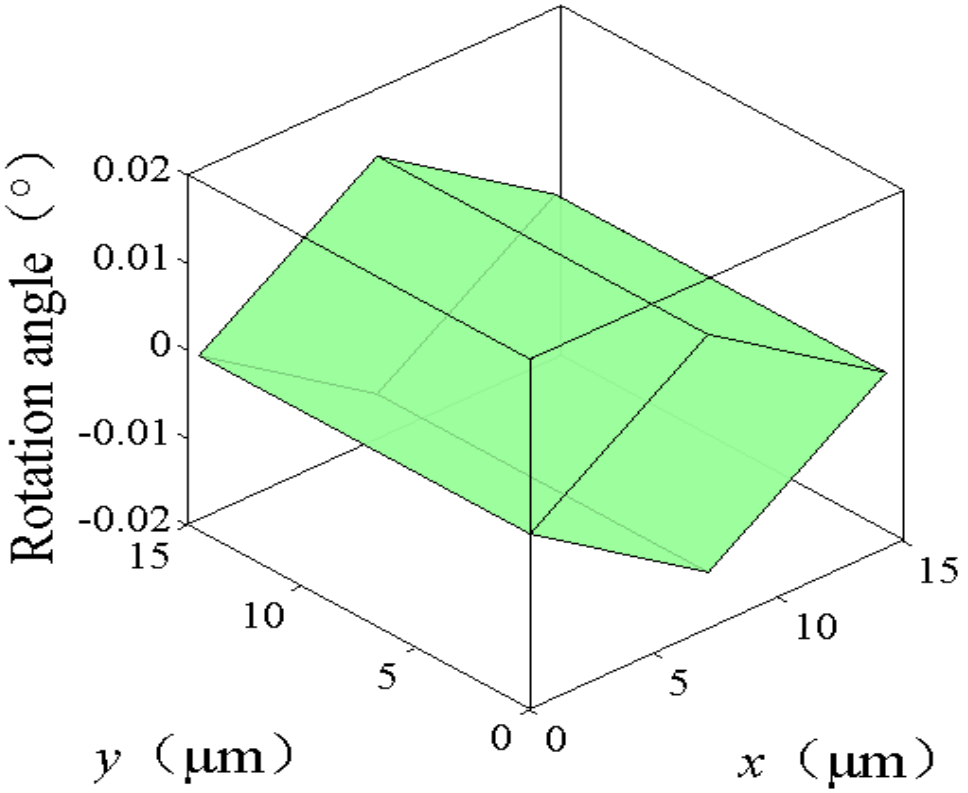

Fig. 5. Workspace of the flexure-based mechanism

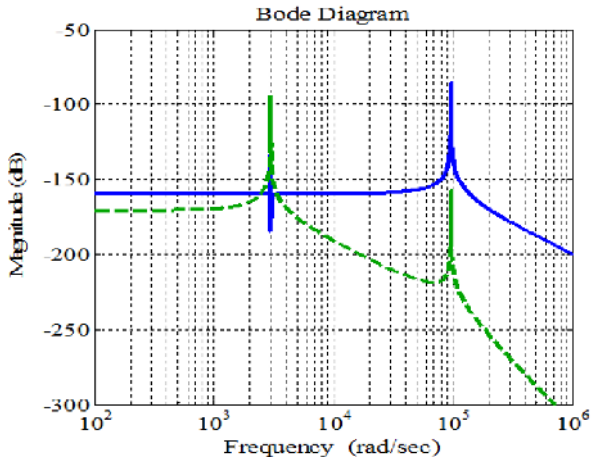

(a) Contact stiffness 1 N/µm

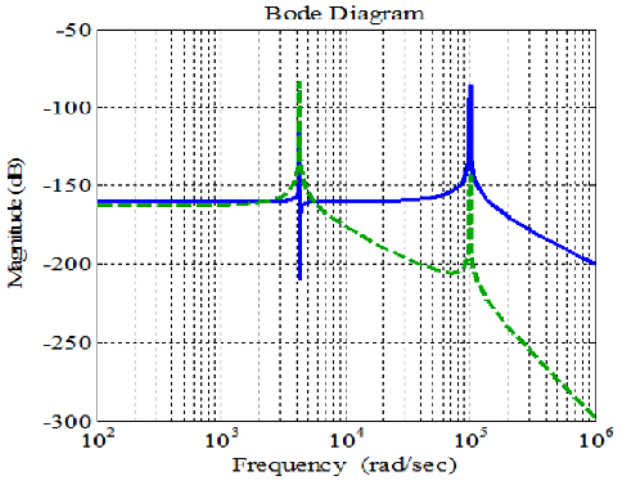

(b) Contact stiffness 5 N/µm

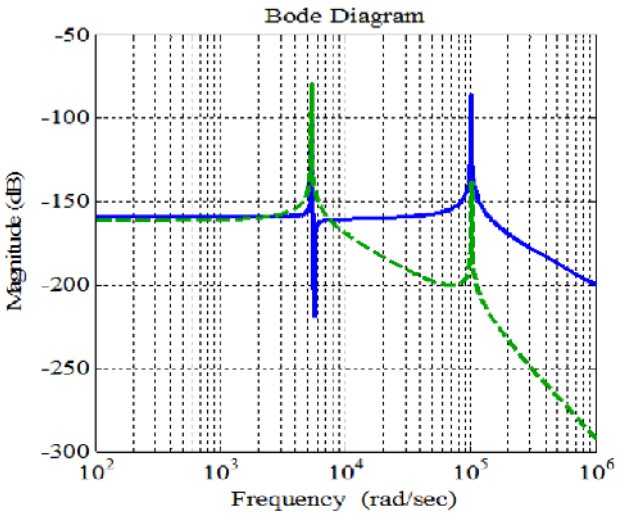

(c) Contact stiffness 10 N/µm

Fig. 6. Bode plot (only magnitude) of different contact stiffness

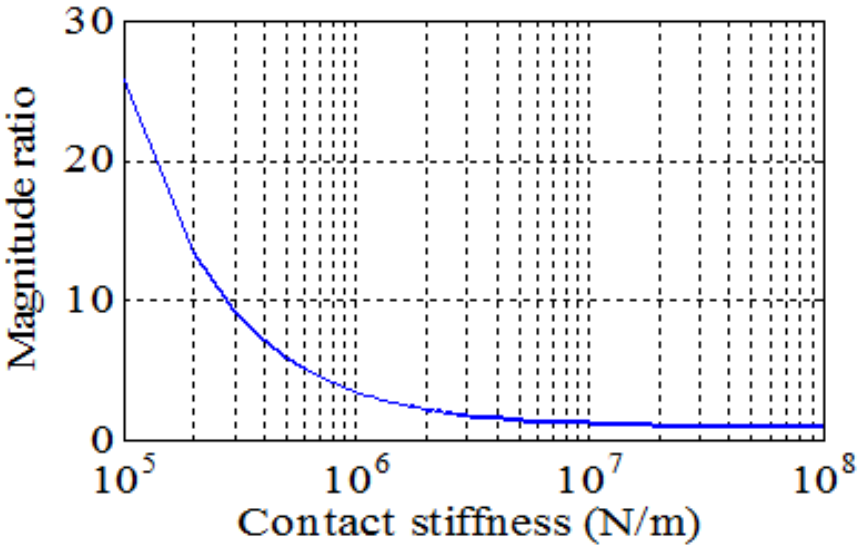

Fig.7. Influence of contact stiffness to the magnitude ratio

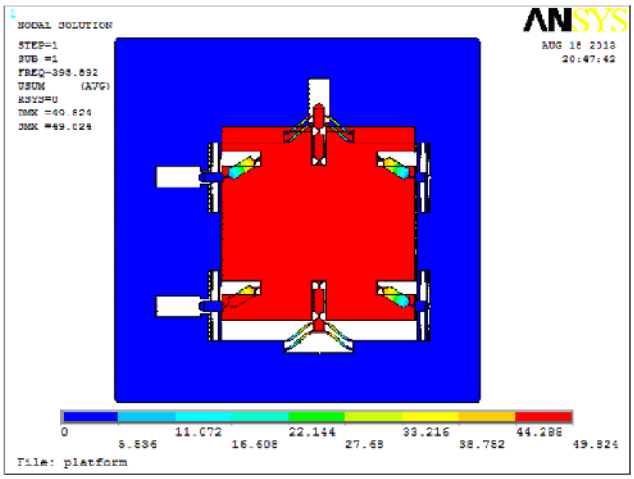

(a) Mode shape in y direction

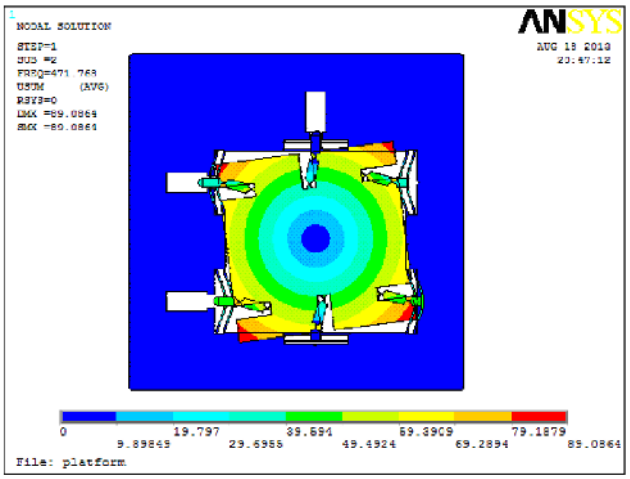

(b) Mode shape in θ_z direction

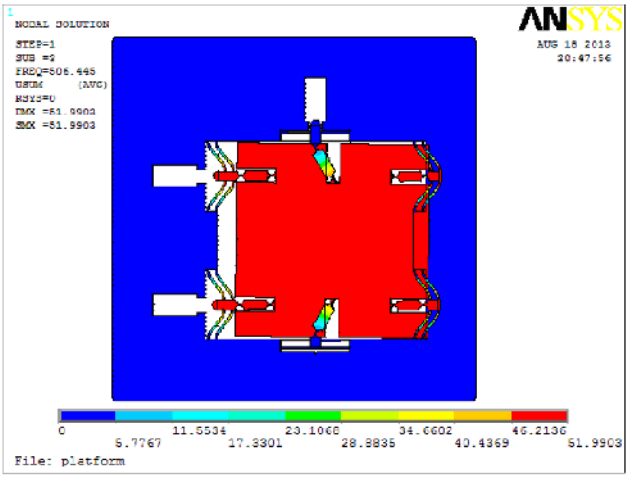

(c) Mode shape in x direction

Fig. 8. Mode shapes of the flexure-based mechanism (without piezoelectric actuators)

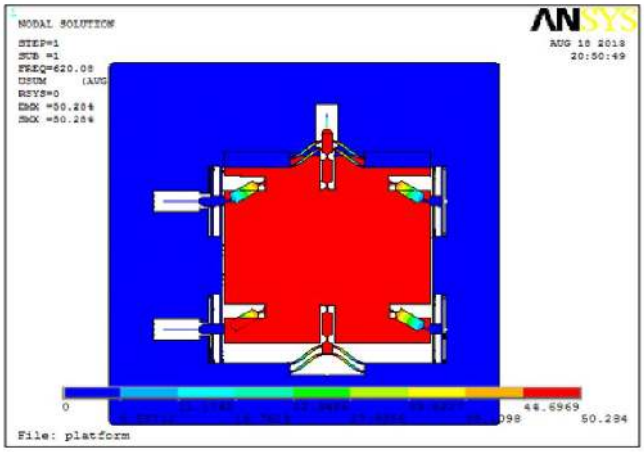

(a) Mode shape in y direction

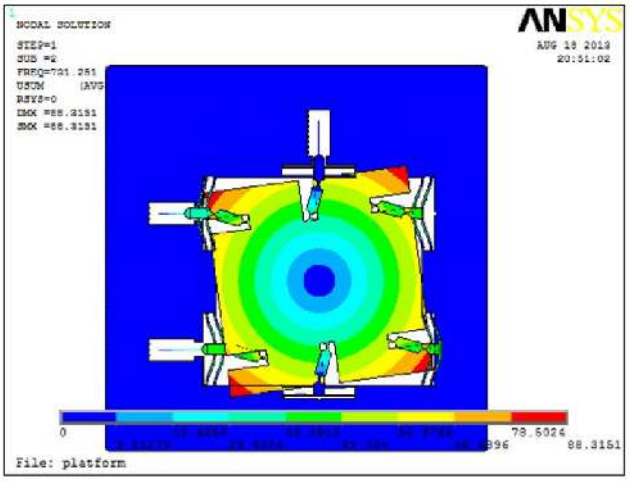

(b) Mode shape in θ_z direction

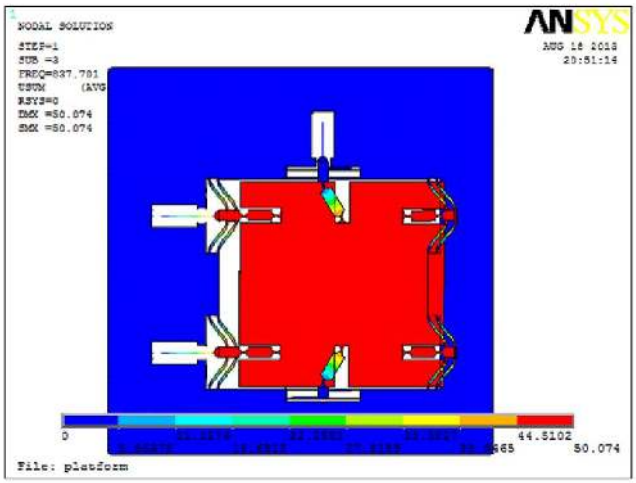

(c) Mode shape in x direction

Fig. 9. Mode shapes of the flexure-based mechanism (with piezoelectric actuators)

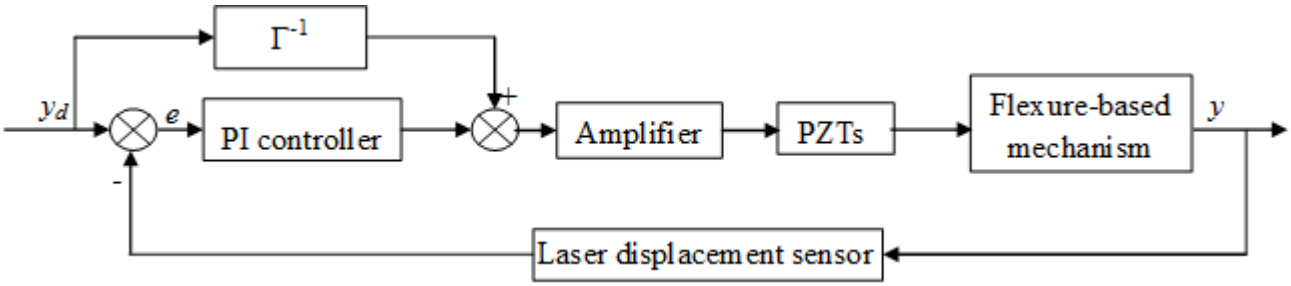

Fig. 10. Block diagram of the feedforward/feedback controller

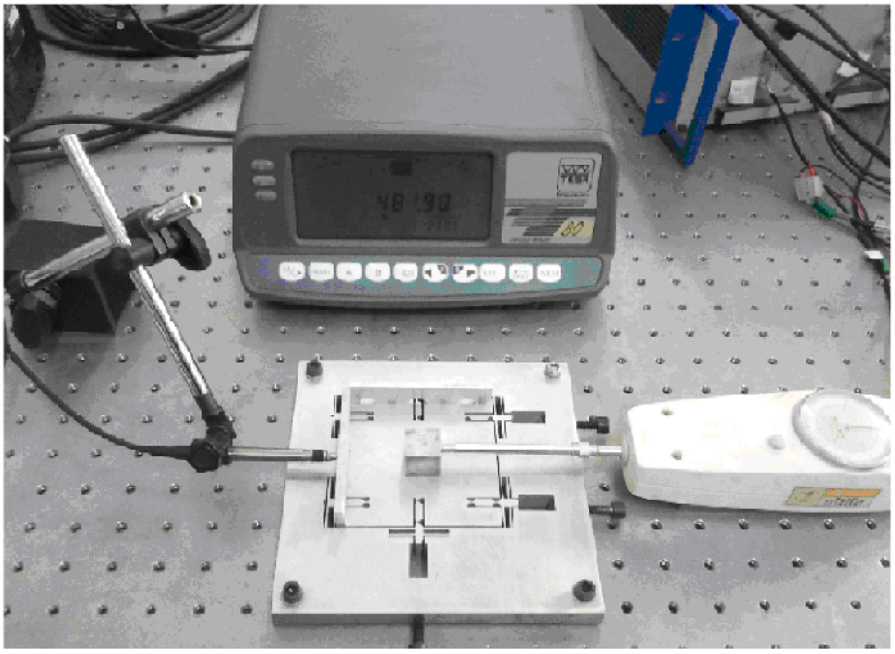

Fig. 11. Stiffness measurement of the flexure-based mechanism

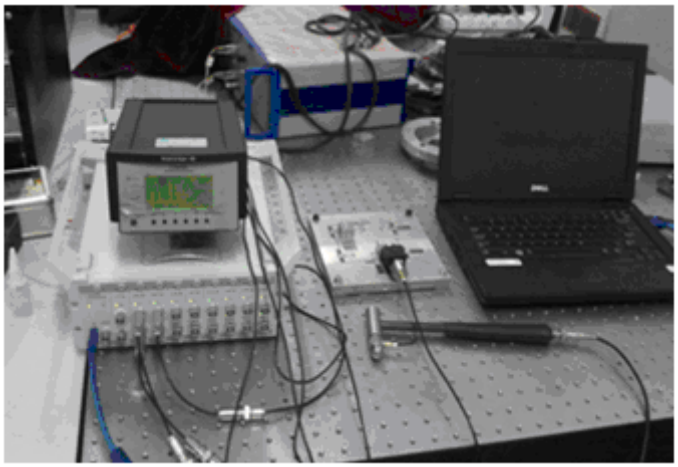

(a) Modal analysis setup

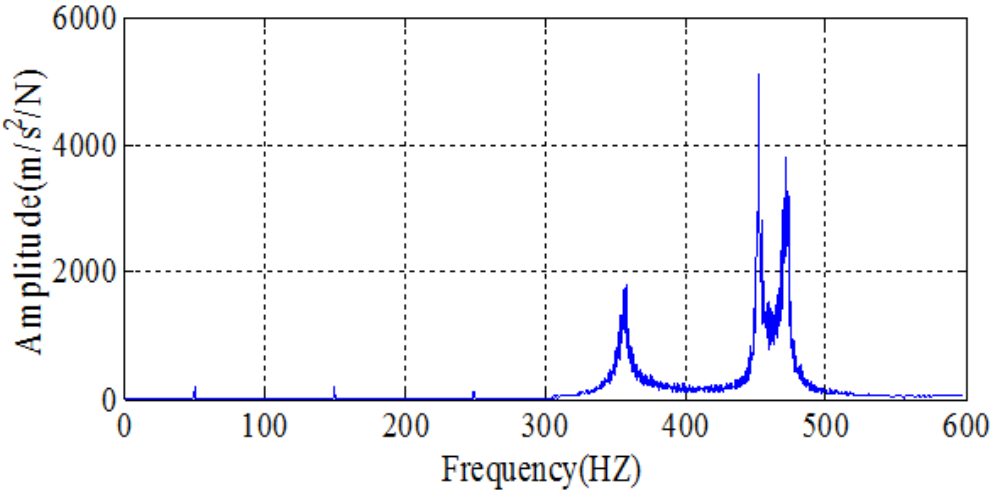

(b) Resonant frequency without actuators

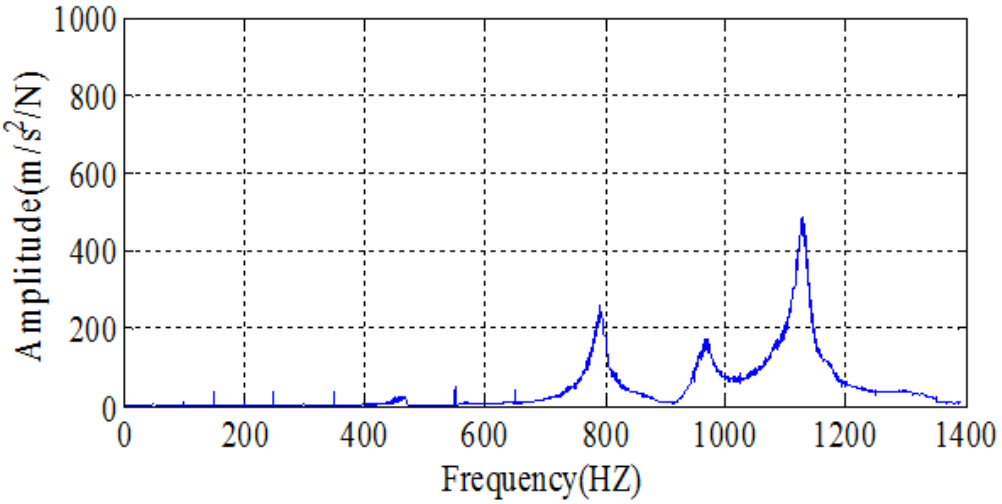

(c) Resonant frequency with actuators

Fig. 12. Modal analysis of the flexure-based mechanism

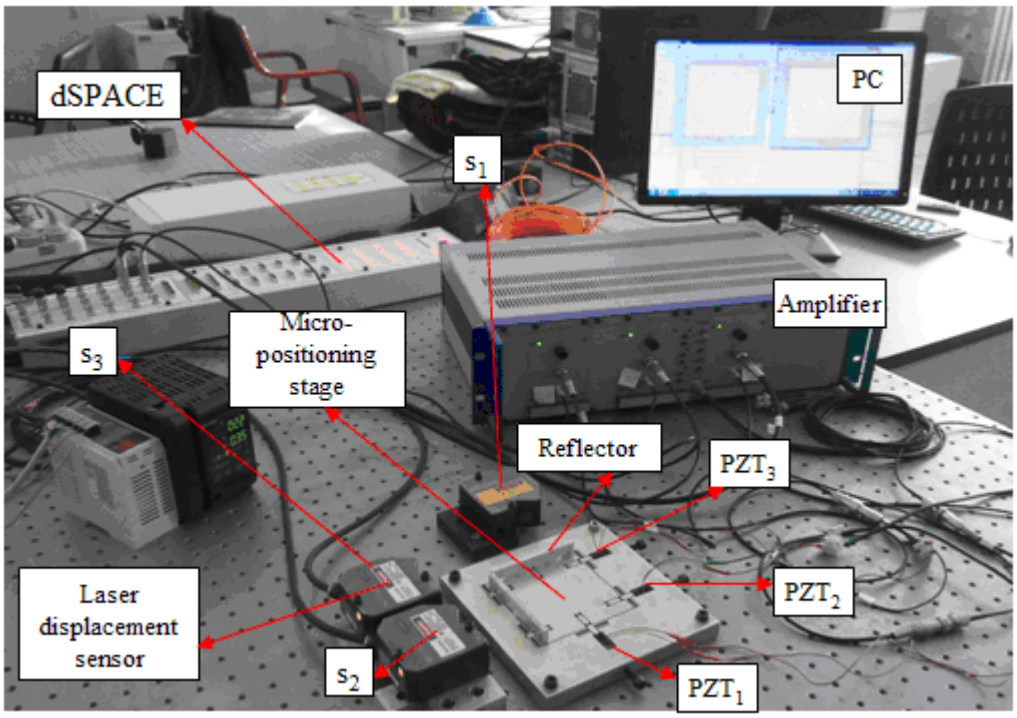

Fig. 13. Control system setup of the flexure-based mechanism

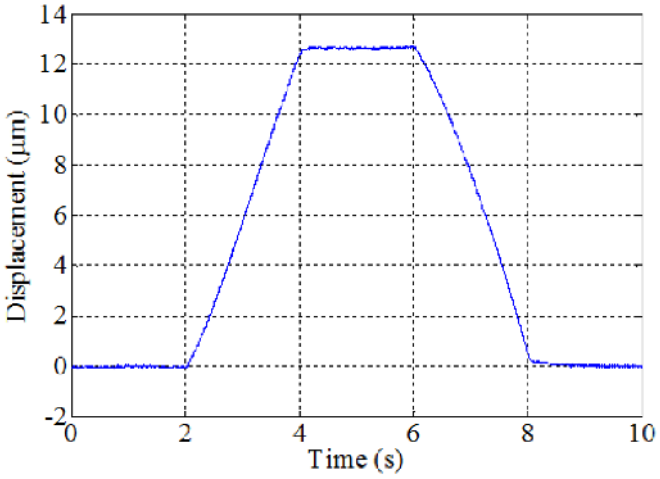

(a) Maximum displacement in x direction

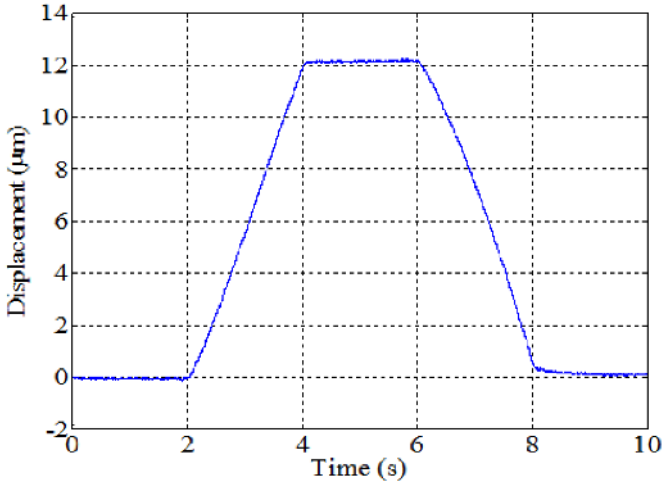

(b) Maximum displacement in y direction

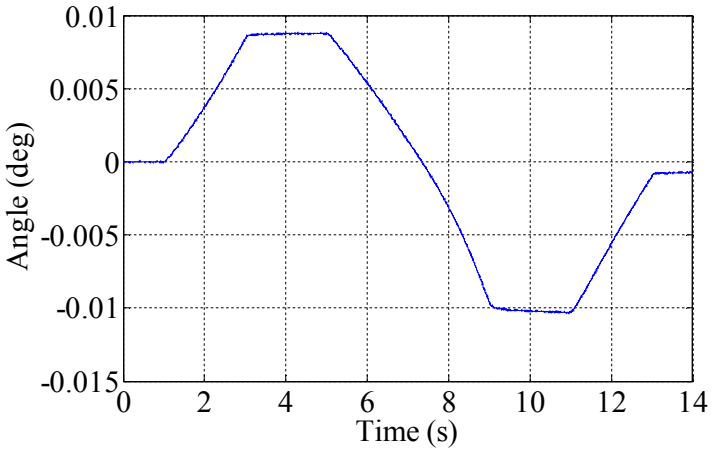

(c) Maximum angle in θ_Z direction

Fig. 14. Open loop travel range of the stage.

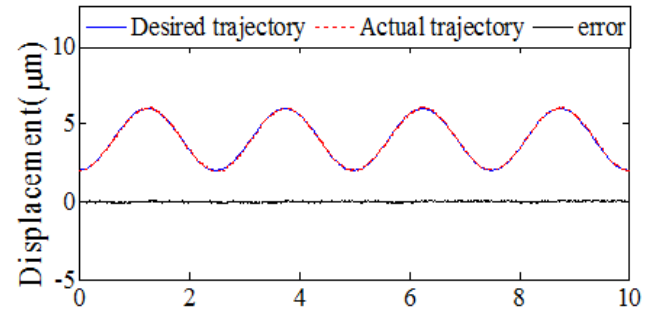

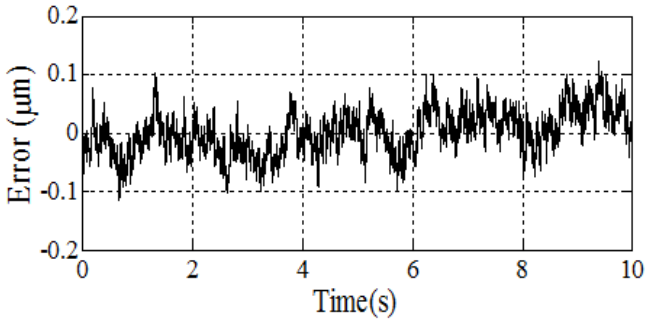

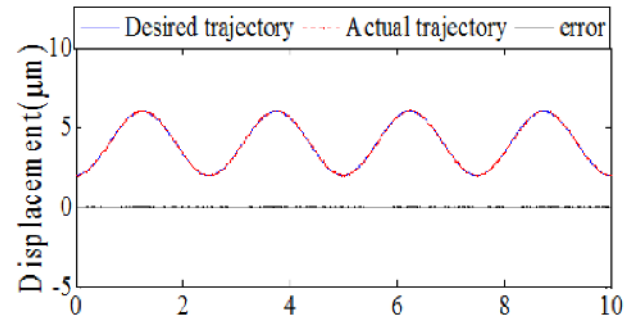

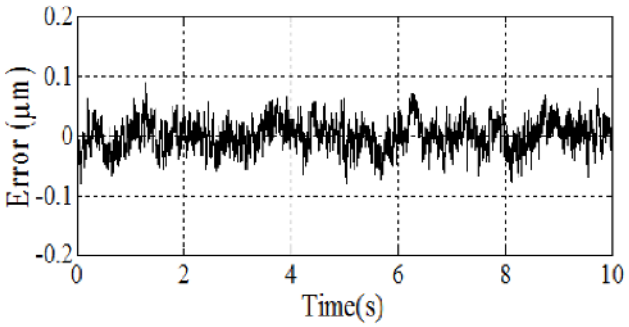

(a) feedforward controller

(b) feedforward/feedback controller

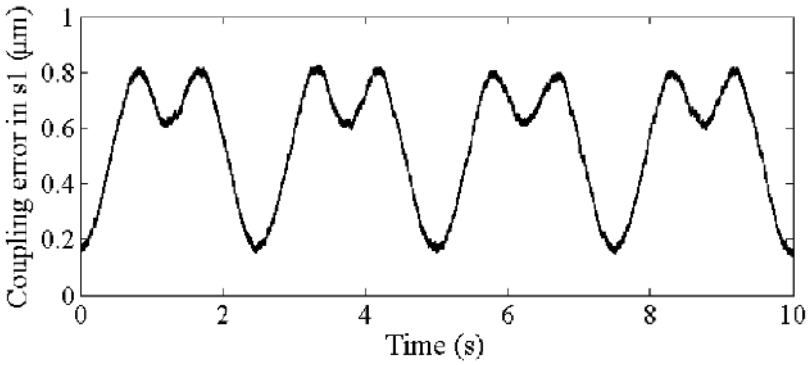

(c) Coupling error in *y* direction

Fig. 15. Trajectory track of a sinusoidal input in *x* direction

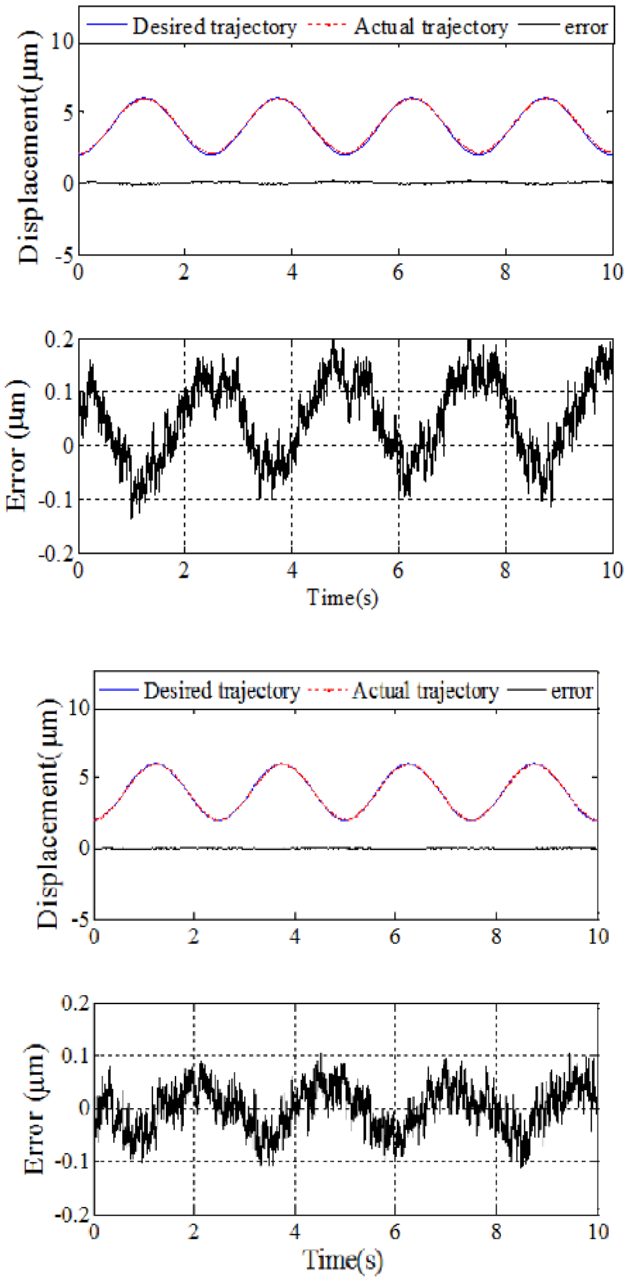

(a) Feedforward controller

(b) Feedforward/feedback controller

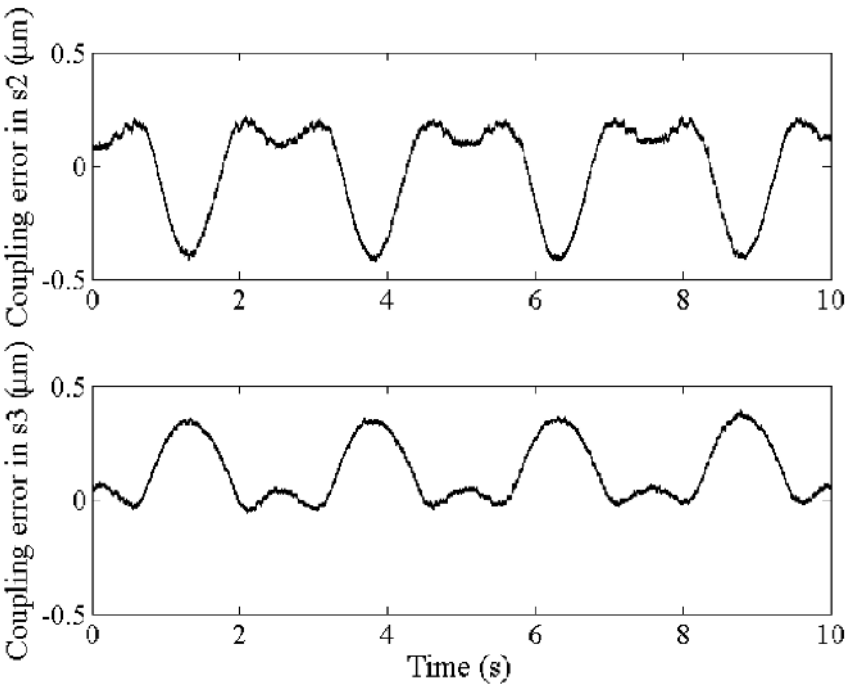

(c) Coupling error in *x* direction

Fig. 16. Trajectory track of a sinusoidal input in *y* direction

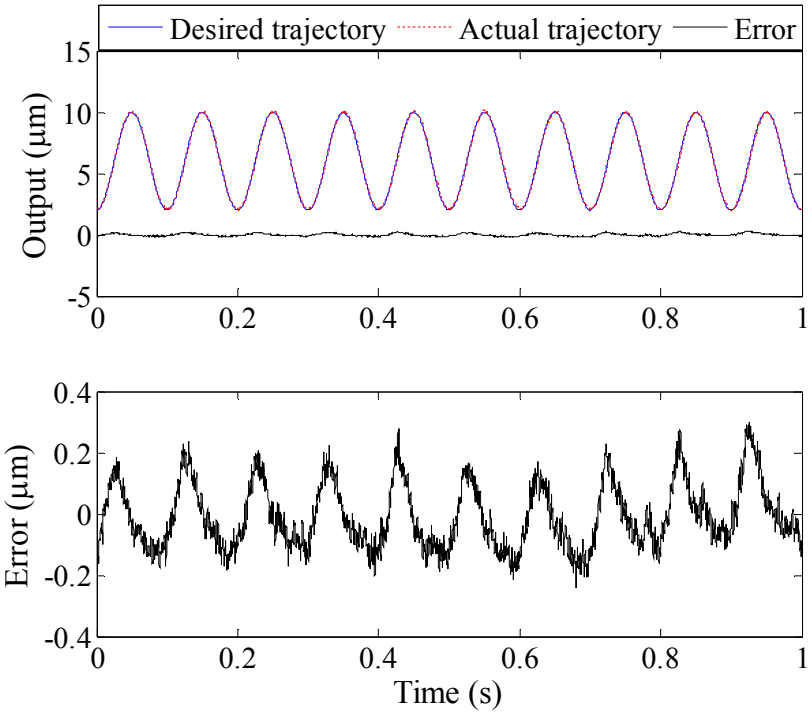

(a) Feedforward controller

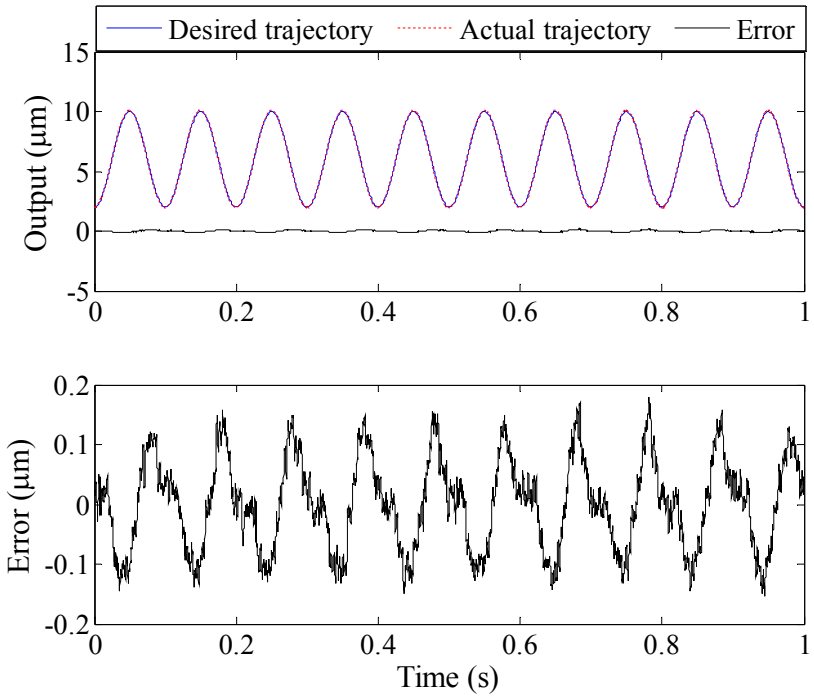

(b) Feedforward/feedback controller

Fig. 17. Trajectory track of a sinusoidal input in *y* direction with a higher frequency (10HZ)

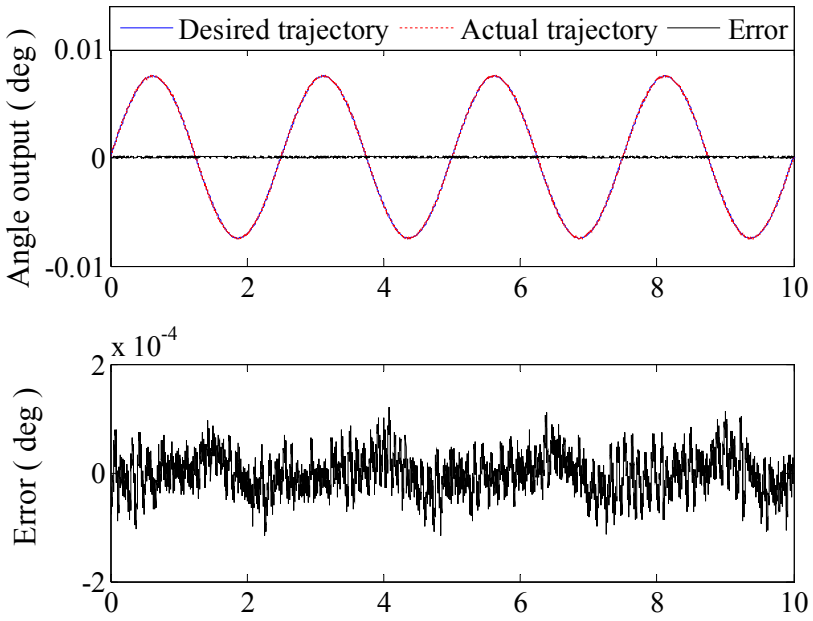

Fig. 18. Trajectory track of a rotation signal

Table 1 The optimization structure size

t_1(mm)	L_1(mm)	t_2(mm)	L_2(mm)	R(mm)
0.9	15	0.8	15	3

Table2 Stiffness and resonant frequencies of the stage without actuators

frequency	Analytical	FEM	Experiment	Error (%)	
				analytical	FEM
K_x (N/μm)	4.2482	4.2351	4.2265	0.51	0.20
K_y (N/μm)	2.4813	2.5293	2.4885	-0.29	1.64
$K_{\theta z}$(Nm/rad)	4252.0	4629.4	4351.1	-2.28	6.38
f_x (HZ)	516.19	506.44	472.11	9.15	7.27
f_y (HZ)	394.50	395.89	357.97	10.20	10.59
$f_{\theta z}$ (HZ)	447.69	471.77	452.88	-1.15	4.17